Low-latitude Ionospheric Research using the CIRCE Mission: Science Overview

K. F. Dymond, A. C. Nicholas, S. A. Budzien, and A. W. Stephan
Space Science Division
Naval Research Laboratory
Washington, DC 20375-5352

Abstract

The Coordinated Ionospheric Reconstruction Cubesat Experiment (CIRCE) is a dual-satellite mission consisting of two 6U CubeSats actively maintaining a lead-follow configuration in the same orbit with a launch planned for the 2018-2019 time-frame. These nanosatellites will each feature two 1U ultraviolet photometers, observing the 135.6 nm emission of atomic oxygen at nighttime. The primary objective is to characterize the two-dimensional distribution of electrons in the orbital plane of the vehicles with special emphasis on studying the morphology of the Equatorial Ionization Anomaly (EIA). The methodology used to reconstruct the nighttime ionosphere employs continuous UV photometry from four distinct viewing angles in combination with an additional data source, such as in situ plasma density measurements or a wide-band beacon data, with advanced image space reconstruction algorithm tomography techniques. The COSMIC/FORMOSAT-3 (CF3) constellation featured six Tiny Ionospheric Photometers, compact UV sensors which served as the pathfinder for the CIRCE instruments. The TIP instruments on the CF3 satellites demonstrated detection of ionospheric bubbles before they had penetrated the peak of the F-region ionosphere, showed the temporal evolution of the EIA, and observed a Medium Scale Travelling Ionospheric Disturbance. We present our mission concept, simulations illustrating the imaging capability of the sensor suite, and a range of science questions addressable using such a system.

1. Introduction

The primary objective of the Coordinated Ionospheric Reconstruction Cubesat Experiment (CIRCE) is to provide space-based tomographic specification of electron density versus altitude and orbit phase angle derived from ultraviolet (UV) observations of the ionosphere with different viewing angles from a pair of cubesats. The primary mission objective permits us to characterize and study the two-dimensional distribution of electrons in the orbital plane of the vehicles with special emphasis on the morphology of the Equatorial Ionization Anomaly (EIA). The experiment consists of two 6U cubesats flying in a tandem lead/trail configuration in coplanar orbits to collect ionospheric measurements optimized for tomographic reconstruction. The two satellites will contain four (2 per satellite) Triple Tiny Ionospheric Photometers (Tri-TIPs), which will observe the 135.6 nm emission that is a key signature produced by the decay of the nighttime F-region ionosphere. The proposed viewing geometry requires a long baseline easily provided in orbit so that the same volume near the peak of the F-region ionosphere, typically at a height 350 km, is simultaneously observed by two satellites separated by ~500 km. The mission is planned to launch into a circular orbit at ~650 km altitude with an inclination between 30° and 60°. The current plan is to launch the pair of satellites using the United States Air Force Space Test Program. The Tri-TIP instruments are envisioned to fly along with a secondary ionospheric sensing payload that has not yet been determined. Figure 1 shows the satellite configuration and the internal layout of the photometers.

The proposed CIRCE satellite and instrument configuration allows the study of the following science questions. Recent measurements have shown the structure of the EIA to be driven by planetary waves forced by tropospheric weather (REF), leading to the following research studies. What is the global

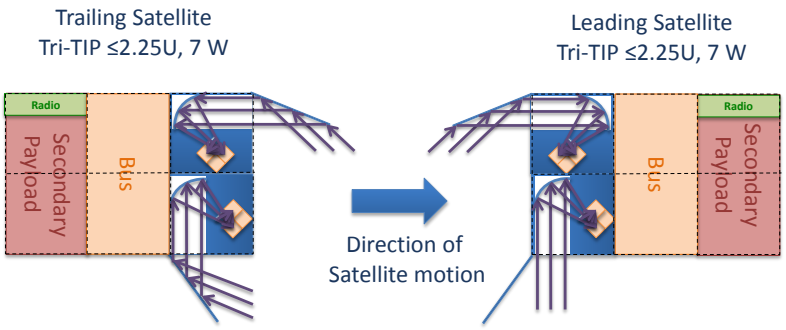

Figure 1: The CIRCE operations concept of two cubesats flying in a lead-trail configuration is shown. Each satellite will carry 2 Tri-TIP UV photometers. Each photometer is equipped with a spring-loaded door that opens once on-orbit; the door has a planar mirror attached to its inner face. The angle that the door opens sets the viewing angle of the photometer. The preliminary concept uses lines-of-sight that are oriented at 45° looking aft, 45° looking forward, 90°, and 22.5° looking aft, where the angles are below the local horizon.

latitude/altitude structure of the EIA? What is driving EIA structure? Which planetary waves are responsible? Which tides are responsible? Measurements made by the Tiny Ionospheric Photometers on the COSMIC-1 mission [*Anthes et al*., 2008; *Dymond et al*., 2017; *Dymond, Nee, and Thomas*, 2000], showed that it is possible to observe Medium-Scale Traveling Ionospheric Disturbances (MSTIDs) using UV photometers. This capability is expected to be replicated in the Tri-TIP sensors), leading to the following research studies. Is it possible to image the altitude/latitude structure of Large-scale Traveling Ionospheric Disturbances and MSTIDs? What is the global distribution of MSTIDs? Is it possible to image the altitude/latitude structure of gravity-wave driven ionospheric perturbations? Additionally, the high sensitivity of the Tri-TIP sensors will permit observations of the low ionospheric densities in the mid-latitude trough. We would like to determine: Is it possible to image the altitude/latitude structure of mid-latitude ionospheric trough? Are there additional ionospheric structures associated with the mid-latitude trough? The TIP sensors on the COSMIC-1 constellation were able to observe ionospheric bubbles before they had penetrated the peak of the F-region ionosphere, leading to the following research studies. Can ionospheric bubbles be tomographically imaged to produce altitude/orbit phase angle cross-sections? Can the bottom-side bubbles be tomographically imaged from above?

This paper describes the CIRCE mission, the proposed photometer concept, and some mission scenarios. We present and discuss the results of some tomography simulations used to assess the mission scenarios and to assess the capabilities of the proposed sensor suite.

2. CIRCE Mission and Instrumentation

Heritage from TIP on COSMIC-1

The Constellation Observing system for Meteorology, Ionosphere, and Climate (COSMIC) also known as Formosa Satellite Mission #3 (FORMOSAT-3) in Taiwan was a 6-satellite constellation developed and flown jointly by the United States of America and the Republic of China (Taiwan). Each of the COSMIC/FOMOSAT-3 (CF3) satellites carried a Tiny Ionospheric Photometer or TIP [*Anthes et al*., 2008; *Dymond et al*., 2017; *Dymond, Nee, and Thomas*, 2000]. The TIP instruments were ultraviolet photometers that operated primarily at nighttime and observed the O I 135.6 nm from atomic oxygen. The Earth's far-ultraviolet nightglow spectrum contains three spectral emissions: H I 121.6 nm, O I 130.4 nm, and O I 135.6 nm. The H I 121.6 nm (Lyman-α) is a bright spectral line that is produced by sunlight scattered from the dayside of the Earth to the nightside by multiple resonant scattering [*Meier*, 1991]. The O I 130.4 nm, and O I 135.6 nm lines are both produced by the same processes (mutual neutralization of O^+ and O^- ions and radiative recombination of O^+ and electrons) that are produced by the decay of the ionosphere. Both emissions are entrapped in the thermosphere by multiple resonant scattering of the spectral lines by atomic oxygen [*Meier*, 1991; *Dymond*, 2009], however, the vertical scattering optical

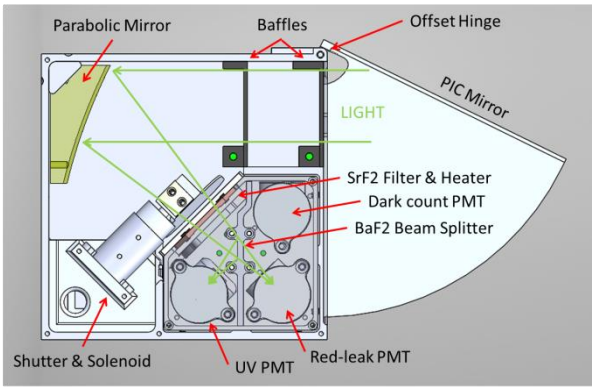

Figure 2: A diagram of a Tri-TIP instrument is shown. Each instrument consists of a "Parabolic Mirror" that feeds three photomultiplier tubes (PMTs) at its prime focus. The instrument simultaneously measures the dark count due to high energy particle flux on-orbit ("Dark count PMT" tube is occluded to seal out any light), the amount of long-wavelength contamination present in the signal ("Red-leak PMT"), and the desired ultraviolet signal ("UV PMT") using three matched PMTs. The "PIC Mirror" is on the inside of the "Dust Cover Door" and is used to select the instrument's viewing direction. The heated strontium fluoride filter ("SrF2 Filter and Heater") eliminates the bright nightglow signatures from atomic hydrogen (H I 1216 Å) scattered to the nightside from the dayside of the Earth and the O I 130.4 nm produced by the natural decay of the ionosphere, a signature that is difficult to interpret due to its large optical depth. The "BaF2 Beamsplitter" is a partially silvered barium fluoride filter that reflects the desired O I 135.6 nm signal (this signal will be contaminated by long-wavelength light) into the "UV PMT" while attenuating the light O I 135.6 nm passing through the filter so that the long-wavelength contamination can be simultaneously monitored by the "Red-leak PMT". The "Shutter and Solenoid" permits blocking of the incoming light to protect the instrument should it inadvertently view the Sun.

depth of the O I 130.4 nm radiation integrated from infinity to the O density peak near 105 km is ~1,000-10,000, which makes interpretation of the emission difficult, while the vertical scattering optical depth of the O I 135.6 nm radiation is ~1 making its interpretation much more tractable. The UV emissions originate only from the ionosphere and, due to absorption of UV light by O_2 and N_2, there is no background radiation.

The TIP instruments consisted of a photometer head that contained a Hamamatsu sub-miniature photomultiplier tube with a magnesium fluoride window and cesium fluoride photocathode at the prime focus of an off-axis parabolic mirror. The TIP instruments attenuated the O I 130.4 nm and H I 121.6 nm emissions using heated strontium fluoride filters. The short wavelength cut-off of strontium fluoride occurs at ~128.0 nm at room temperature, but this cut-off can be shifted to longer wavelengths (132.5 nm) by heating the filter to ~100 C. The long-wavelength edge of the instrumental passband was limited by the response of the cesium iodide photocathodes, which typically are not sensitive to light at wavelengths longer than ~180 nm. However, the TIPs saw city lights and moonlight scattered from clouds indicating that an anomalously high long-wavelength response of the photocathodes was allowing a "red leak" or photons beyond the expected passband to be detected by the instruments. Thus, the COSMIC/TIP measurements were limited to moon-down periods, and the data had to be filtered for city light contamination. Further information regarding the optical design of the COSMIC/TIP instruments, some measurement highlights, and lessons learned are presented in *Dymond et al*. [2016].

CIRCE Experiment Configuration

The Tri-TIP instruments are based on the proven design of the COSMIC/TIP instruments with modifications that permit better characterization of the "red-leak" and high energy particle noise. Figure 2 shows the configuration of the Tri-TIP photometers. The name Tri-TIP is derived from the idea that each instrument contains three photomultiplier tubes (PMTs) so it can simultaneously make the three measurements needed to accurately quantify the nighttime airglow 135.6 nm signal. Each instrument consists of an off-axis parabolic mirror feeding the three PMTs, which are placed at its prime focus. Light

reflected off the parabolic mirror passes through the heated strontium fluoride filter which eliminates the bright nightglow signatures from atomic hydrogen (H I 121.6 nm) and O I 130.4 nm. The short-wavelength filtered UV light then impinges upon a barium fluoride beam splitter, which is a partially silvered barium fluoride filter that reflects approximately one-half of the light into the PMT that measures the O I 135.6 nm emission and allows the remainder of the light to pass through into the red leak PMT. The barium fluoride filter has a short-wavelength cut-off that eliminates the O I 135.6 nm emission, while allowing the red leak signal to pass through. The UV PMT and red leak PMT will both observe the red leak signal. The red leak corrected O I 135.6 nm signal is obtained by appropriately scaling the red leak and dark count signals and subtracting them from the raw UV PMT measurement. A shutter mechanism is included in the instrument so that the beam can be blocked to prevent damage to the instrument should the Sun pass through the instrument's field-of-view. Additionally, by blocking the beam, dark count measurements can be made simultaneously on all three tubes; from these measurements, the dark count scaling factors can be derived.

CIRCE Observation Scenarios

Several observation scenarios were used to assess the ability of the CIRCE mission to determine the ionospheric electron density. The CIRCE mission is expected to launch into a near-circular orbit with an orbit inclination anywhere between 0° and > 90°, depending on the orbital characteristics desired by the primary payload, as cubesats are generally secondary payloads. The simulations considered in this work were exactly polar orbits, at 90° inclination, to assess the ability of the CIRCE mission concept to remotely sense the ionospheric morphology in the EIA and to assess the mission's capability to sense and detect ionospheric bubbles. We chose an orbit inclination of 90° because the ionospheric gradients in the EIA are strongest in the North-South direction and tomography with large gradients is a more stressing test of the concept than tomography in cases with smaller gradients, such as the ionospheric gradients that would be observed in an equatorial orbit. The nominal observation scenario is to have 4 fixed viewing directions. We have developed and evaluated additional scenarios including a limb scanning scenario where the trailing satellite is slowly repeats a pitch-axis scan such that the fields-of-view of the two photometers are scanned though ~15° and a scenario where Langmuir probes to measure the local plasma density are added to both satellites. In this paper, we will focus our discussion on the nominal 4 fixed viewing angles scenario. In this scenario, shown in Figure 3, the lead satellite views in the nadir (red arrow) and aft 45° below the vehicle's local horizon (black arrow). The photometers on the trailing vehicle view ahead of the vehicle one at 45° below the vehicle's local horizon (green arrow) and the second views 22.5° below the vehicle's local horizon (blue arrow), which produces a tangent ray height of ~120 km from a satellite orbiting at 600 km. The instruments are expected to integrate for ~1 s and produce samples every 7.5 km along the orbit track for an angular spacing of ~0.06°.

3. CIRCE Simulations

The CIRCE concept of operations was tested by simulating measurements using realistic viewing geometry, expected instrumental sensitivities, and with realistic instrumental noise superimposed. The full physics of ionospheric 135.6 nm nightglow was simulated including the radiative recombination and mutual neutralization sources that produce the emission; vertical radiation transport, which redistributes the photons in altitude, was also included; and, lastly, radiation transfer along the lines-of-sight was included to account for the loss of photons due to pure absorption and resonant scattering during their transit from the source region to the observer. The inversion of the simulated "data" was performed using the newly developed Volume Emission Rate Tomography (VERT) code [*Dymond, Budzien, and Hei*, 2017]. This approach produces the volume emission rate consistent with the measurements and is a general approach for interpreting optical tomography data. When using VERT, additional modeling is often needed to convert the volume emission rate to physical quantities, such as electron density.

Physics of the 135.6 nm Emission

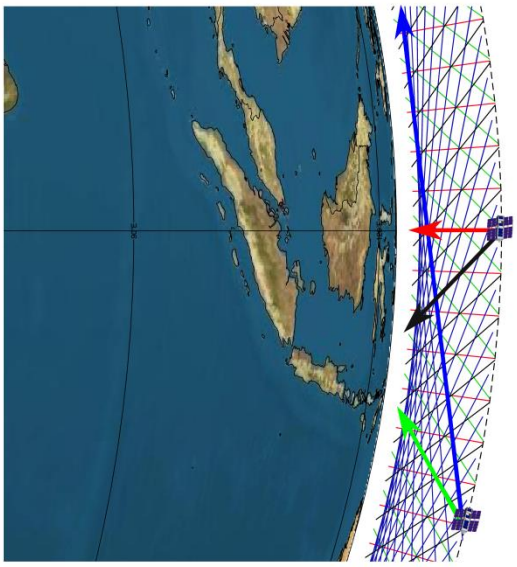

Figure 3: The nominal observation scenario is shown. The lead satellite views in the nadir (red arrow) and aft 45° below the vehicle's local horizon (black arrow). The photometers on the trailing vehicle view ahead of the vehicle one at 45° below the vehicle's local horizon (green arrow) and the second views 22.5° below the vehicle's local horizon (blue arrow), which produces a tangent ray height of ~120 km from a satellite orbiting at 600 km. The red, green, blue and black lines crossing the orbit plane represent additional lines-of-sight; for clarity, the spacing between observations is 2° of orbit phase angle. The instruments are expected to integrate for ~1 s and produce samples every 7.5 km along the orbit track for an angular spacing of ~0.06°. The dashed line is the satellite orbit and the satellites would move from bottom to top in the figure.

The 135.6 nm emission is produced in the nighttime ionosphere by two reactions. Radiative recombination is the chemical recombination of O^+ ions with electrons resulting in a neutral oxygen atom in an excited electronic state that decays to the ground state with the emission of a photon, *viz*:

$$O^+ + e^- \rightarrow O^*(^5S) \rightarrow O\,(^3P) + h\nu\ (135.6\ nm)$$

The second reaction is mutual neutralization of O^+ ions and O^- ions; the O^- ions are created by radiative attachment of an electron to a neutral oxygen atom to create the anion. The reaction chain is:

Radiative Attachment: $O + e^- \rightarrow O^- + h\nu$ (Long wavelength infrared)

Ion-atom Neutralization: $O^- + O \rightarrow O_2 + e^-$

Mutual Neutralization: $O^+ + O^- \rightarrow O + O^*(^5S) \rightarrow 2O\,(^3P) + h\nu\ (135.6\ nm)$

The volume emission rate, ε_0, for these two reactions is given by:

$$\varepsilon_0(z) = \gamma\ \beta_{1356}\frac{k_1 k_2 n_e(z) n_O(z) n_{O^+}(z)}{k_2 n_{O^+}(z) + k_3 n_O(z)} + \gamma\ \alpha_{1356} n_e(z) n_{O^+}(z) \qquad (1)$$

where the first term is the volume emission rate for mutual neutralization and the second term is the volume emission rate for radiative recombination. The reaction rate coefficients can be found in *Melendez-Alvira et al.* [1999] and n_e, n_O, and n_{O^+} are the electron, oxygen, and O^+ densities, respectively. In our simulations below, the O density is taken from the NRLMSISE-00 model [*Picone et al*., 2002] and the electron density is taken from the International Reference Ionosphere–2007 [*Bilitza and Reinisch*, 2008]. In the nighttime F-region ionosphere, the electron and O^+ densities are equal, so that the electron density can be used in place of the O^+ density when calculating the volume emission rate. This expression is used to calculate the initial volume emission rate, ε_0. The photons initially created are redistributed in altitude by multiple resonant scattering with O atoms. This is modelled in the Complete Frequency Redistribution Approximation [*Meier*, 1991; *Dymond et al.*, 1997].

Radiation Transport

The photons initially created are redistributed in altitude by multiple resonant scattering with O atoms which redistributes the photons both horizontally and vertically. However, the horizontal O density gradients are much lower than the vertical density gradients so most of the redistribution is vertical and the plane-parallel approximation has been shown to accurately model the transport process. The 135.6 nm emission originates in the ^5S upper state while the ground state of atomic oxygen is the ^3P state causing the transitions between these states to be spin-forbidden. The 135.6 nm emission is a doublet with wavelengths of 135.6 and 135.8 nm. Both lines are resonantly scattered by atomic oxygen and absorbed by molecular oxygen. The resonant scattering redistributes the photons both horizontally and vertically. However, the horizontal density gradients are much lower than the vertical density gradients so most of the redistribution is vertical and the plane-parallel approximation has been shown to accurately model the transport process. The line center scattering cross-sections for the scattering are: 2.499×10^{-18} cm^2 (135.6 nm) and 1.242×10^{-18} cm^2 (135.8 nm) [*Meier*, 1991], and thus the optical depth for the 135.6 nm emission is approximately twice the optical depth of the 135.8 nm emission. Photons are absorbed by molecular oxygen in the Schumann-Runge continuum [*Meier*, 1991]. The absorption cross-sections are: 7.20×10^{-18} cm^2 (135.6 nm) and 7.15×10^{-18} cm^2 (135.8 nm) [*Wang et al.*, 1987]. The scattering optical depth of the 135.6 nm emission integrated from infinity to the altitude where the O density peaks, ~105 km, approaches ~1. This permits the radiation transport to be modeled in the computationally fast Complete Frequency Redistribution Approximation [*Meier*, 1991; *Dymond et al.*, 1997]. Furthermore, when modeling the nighttime radiation transport, the atmosphere can be treated as isothermal with little loss in accuracy.

In this work, the radiation transport is modeled using the integral version of the radiation transport equation in the plane-parallel Complete Frequency Redistribution approximation [*Meier*, 1991; *Dymond et al.*, 1997; *Dymond*, 2009]. The integral equation for the photon transport is:

$$\varepsilon(z) = \varepsilon_0(z) + n_O(z)\sigma \int_{z_{min}}^{z_{max}} \varepsilon(z') H\left(|\tau(z) - \tau(z')|, |t(z) - t(z')|\right) dz' \qquad (2)$$

where z_{max} and z_{min} are the upper and lower limits of the altitude, typically 1000 km and 90 km, respectively, and ε is the volume emission rate. The optical depths for scattering and absorption are:

$$\tau(z) = \sigma \int_z^\infty n_O(z') dz'$$

$$t(z) = \sigma_{O_2}^{abs} \int_z^\infty n_{O_2}(z') dz'$$

The Holstein H function is the probability that a photon originating altitude z′ altitude reaches altitude z integrated over the entire plane perpendicular to z:

$$H(\tau, t) = \frac{1}{2\sqrt{\pi}} \int e^{-2x^2} E_1\left(\tau e^{-x^2} + t\right) dx$$

The integration is carried out over all photon frequencies, x. The function, E_1, is the exponential integral function of the first kind. Equation 2 is a Fredholm integral equation of the first kind. This equation is typically solved by discretization in z and then assuming that the volume emission rate is approximately constant over the z layers and the integrals of the Holstein function are evaluated over the layers. This procedure results in a system of equations that is solved by matrix inversion.

Radiation Transfer

Once the photons are created and then scattered or redistributed in altitude, one needs to model the transfer of that radiation from its source to the observer. The equation for the 135.6 nm brightness is:

$$I_{1356} = 10^{-6} \sum \int_0^{\infty} T(|\tau(s) - \tau(0)|, |t(s) - t(0)|)\ \varepsilon\big(z(s), \varphi(s)\big)\, ds \tag{3}$$

where the summation is carried out over the two lines in the doublet because the SSULI instrument cannot spectrally resolve them. The constant, 10^{-6}, converts the brightness to units of Rayleighs (R). The Holstein transmission function or T-function is defined:

$$T(\tau, t) = \frac{1}{\sqrt{\pi}} \int_{-\infty}^{\infty} e^{-x^2} \exp(-\tau e^{-x^2} + t) dx$$

where x, denotes the frequency in Doppler units. Equation 3 is another example of a Fredholm integral equation of the first kind. To solve for the volume emission rate in a tomographic sense, the equation is normally discretized into voxels where the volume emission rate is assumed to be constant. Then, the system is solved to infer the volume emission rate. In this work, we assume that the volume emission rate varies bi-cubically and use bi-cubic splines to discretize the integrals; this approach results in a smoother solution for the volume emission rate field. The following system of equations is solved using the VERT approach:

$$I_{1356} = 10^{-6} \sum W_i G_i \varepsilon(z_i, \varphi_i)\, T(|\tau(s_i) - \tau(0)|, |t(s_i) - t(0)|) \Delta s_i \tag{4}$$

where s_i is the path-length from the observer to the i^{th} point ion the line-of-sight, z_i is the altitude, φ_i is the latitude, G_i is the quadrature weight, W_i is the bi-cubic spline weighting, and Δs_i is the differential path length along the line-of-sight.

VERT Technique

Equation 4 is solved using the VERT technique a fast, non-negative iteration based on the Richardson-Lucy algorithm [*Richardson*, 1972; *Lucy*, 1974; *Dymond, Budzien, and Hei*, 2015, 2017]. The Richardson-Lucy algorithm seeks log-likelihood solution based on Poisson statistics, which is necessary as the SSULI measurements are based on photon counting and therefore contain photon shot or Poisson noise. The VERT approach uses a physicality constraint applied between iterations to smooth or regularize the solution. We regularize to the isotropic diffusion equation between steps [*Dymond, Budzien, and Hei*, 2015, 2017] and have found this method outperforms Maximum A Posteriori (MAP) and Tikhonov regularization approaches and converges very rapidly. The VERT approach was validated in previous work using SSULI measurements at 91.1 nm [*Dymond et al*., 2015, 2017a] and electron density measurements made by the Advanced Research Project Agency Long-range Tracking and Identification Radar (ALTAIR) [*Tsunoda et al*., 1979].

Inversion Approach

Once we have simulated a set of CIRCE measurements, we use the VERT technique to solve equation 4 to produce the 2D distribution of photon emission in the orbit plane. We account for radiation transfer due to resonant scattering and pure absorption in the path-length matrices used in VERT inversions. The NRLMSISE-00 model was used to estimate the O and O_2 densities used in the radiation transfer and radiation transport calculations. After the VERT inversions are performed, we have the volume emission rate including radiation transport, ε. Equation 2 is solved to remove the resonant scattering contribution to the volume emission rate and infer the initial volume emission rate, ε_0. Then equation 1 is solved using

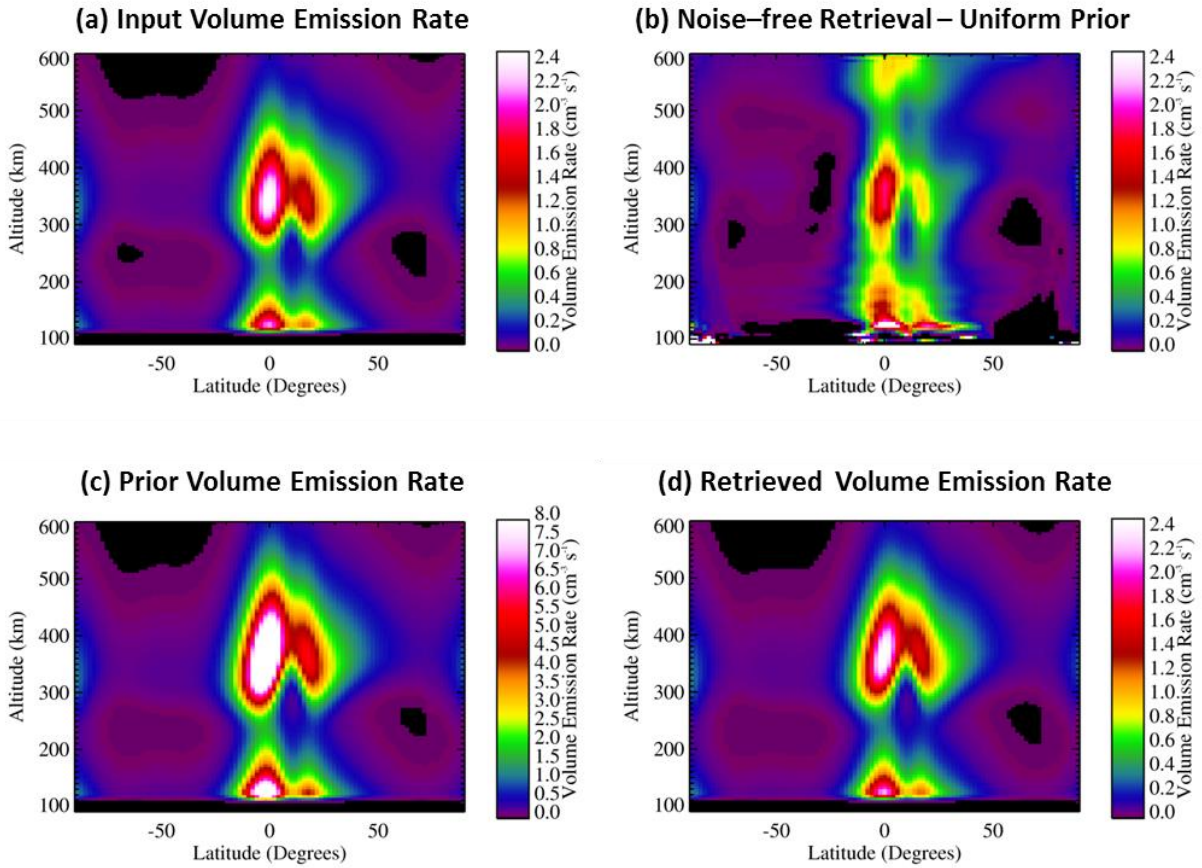

Figure 4: The volume emission rate of the Nighttime Ionosphere is shown. Panel (a) shows the volume emission rate used to simulate the "data". Panel (b) shows the retrieved volume emission rate using a uniform prior; clearly the measurement scenario and VERT technique are unable to uniquely retrieve the ionosphere in this case. Panel (c) shows the prior ionosphere used; this ionosphere has a structure that is similar to the input ionosphere but has a higher magnitude ~3x the initial volume emission rate. Panel (d) shows the retrieved volume emission rate initialized with the prior from panel (c). The agreement is greatly improved. Note: the enhancements at the bottom of each panel, near 110 km, are due to the entrapment of the photons by multiple resonant scattering.

Newton-Raphson iteration [*Press et al*., 1992] to determine the electron density, which is compared to the ALTAIR results.

CIRCE VERT Simulations

The CIRCE concept of operations was tested by simulating measurements using realistic viewing geometries, expected instrumental sensitivities, and with realistic photon shot noise superimposed. The standard operational mode of the CIRCE mission is to have the two satellites in a 600 km altitude circular orbit with the two satellites in a lead-trail configuration and a nominal separation of ~250 km. Figure 3 shows a diagram of the proposed nominal sensor configuration. The lead satellite views in the nadir (red arrow) and aft 45° below the vehicle's local horizon (black arrow). The photometers on the trailing vehicle view ahead of the vehicle: one at 45° below the vehicle's local horizon (green arrow) and the second views 22.5° below the vehicle's local horizon (blue arrow), which produces a tangent ray height of ~120 km from a satellite orbiting at 600 km. The red, green, blue and black lines crossing the orbit plane represent additional lines-of-sight; for clarity, the spacing between observations is 2° of orbit phase angle. The instruments are expected to integrate for ~1 s and produce samples every 7.5 km along the orbit track for an angular spacing of ~0.06°. The vehicle separation was chosen so that the nadir line-of-

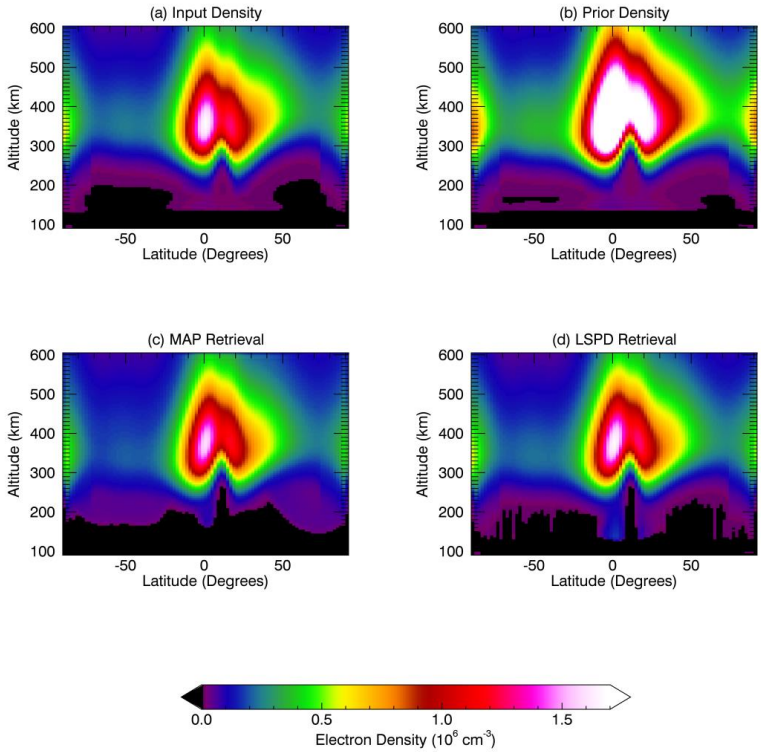

Figure 5: The electron densities for the first simulation using a nominal IRI-2007 ionosphere are shown. Panel (a) shows the input electron density. The prior density used in the inversions is shown in panel (b); as noted above, this prior has a similar structure to the Input Density but a much larger magnitude. The MAP retrieval is shown in panel (c) and the LSPD retrieval is shown in panel (d). The MAP retrieval is similar to the LSPD retrieval and reflects that the assumed uncertainty assumed for the model was too large and therefore the retrieval was driven by the LSPD algorithm and the measurement uncertainties.

sight of the lead vehicle is intersects the 45° line-of-sight of the photometer on the trailing vehicle at an altitude of 350 km, the canonical ionospheric peak height. In addition to the nominal observation scenario, several additional observational scenarios were evaluated. One scenario included Langmuir Probes aboard each satellite to measure the plasma density at the satellite altitude. An additional scenario had the trailing satellite slowly executing a saw-tooth pitch axis scan (by convention, the pitch-axis is perpendicular to the orbit plane) through 23° to provide a slow limb scan in the orbit plane. Due to length constraints in the proceedings, we will focus the discussion only on the nominal observation scenario.

Two ionospheric simulations were used to assess the CIRCE observational scenarios. The first simulation was of a nominal, bubble-free IRI-2007 ionosphere at solar maximum conditions (10.7 cm solar flux = 200×10^{-22} W cm^{-2} Hz^{-1}) at 0° longitude at local midnight (0 UT) on 21 September. The full model included radiation transport. The second simulation superimposed ionospheric bubbles upon the background IRI-2007 ionosphere, however in this simulation radiation transport was not performed to better assess whether the bubbles could be resolved. We found that inclusion of the radiation transport caused the contrast of the bubble depletions to decrease as photons were scattered from nearby regions into the bubbles. Both simulations were for polar orbits of the CIRCE satellites. The simulations then used the observation scenarios to generate synthetic data, which then had realistic photon shot noise superimposed. We assumed that the sensitivity of the photometers was 100 ct/s/R, which is lower than the expected sensitivity. The exception to this were the limb photometers, which were assumed to have smaller fields-of-view and consequently the sensitivities of the limb sensors was 10 ct/s/R. This lower sensitivity would produce comparable signal-to-noise ratios as the downward-looking photometers because of the limb-brightening due to the limb viewing geometry.

4. Simulation Results

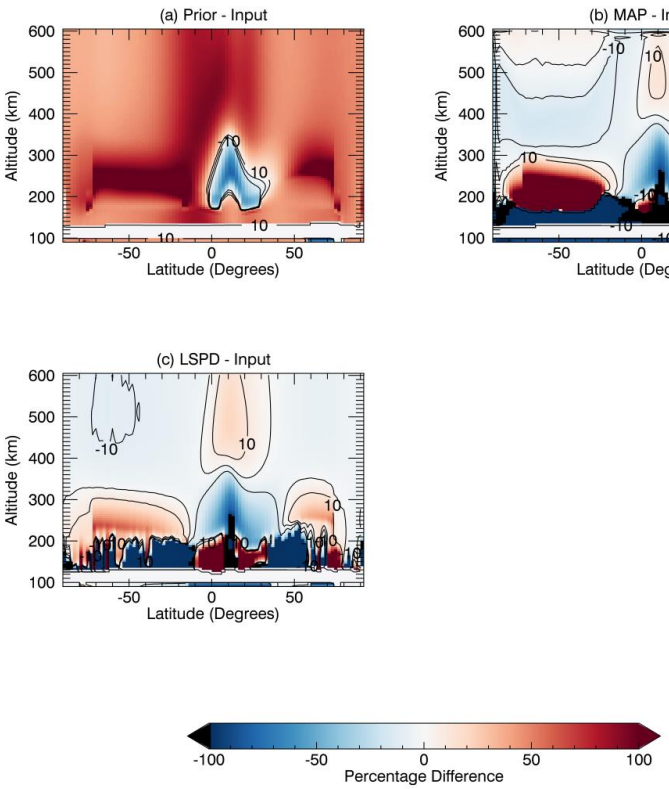

Figure 6: The percentage differences between the input electron density and the prior, LSPD retrieval, and MAP retrievals are shown for the first simulation using a nominal IRI-2007 ionosphere. Panel (a) shows the (Prior – Input electron density) divided by the input electron density. The prior electron density was larger everywhere except in the valley below the magnetic equator indicated by the blue region. The contours in the images are at -10%, 0%, and +10%. The percentage difference between the MAP retrieval and input density is shown in panel (b) and the percentage difference between LSPD retrieval and the input density is shown in panel (c). The LSPD retrieval is within ±10% of the input density almost everywhere except, most notably, on the bottomside.

Figure 4 shows the volume emission rate of the Nighttime Ionosphere for the first simulation using the nominal, bubble-free IRI-2007 ionosphere. In each panel, there is an enhancement at the bottom, near 110 km, caused by the entrapment of the photons due to multiple resonant scattering. The two enhancements at ~350 km altitude and 0 and 20° latitude are the Equatorial Ionization Anomaly crests. Panel (a) shows the volume emission rate used to simulate the "data". Panel (b) shows the retrieved volume emission rate using a uniform prior and noise-free "data", which should represent the best case inversion; clearly the measurement scenario and VERT technique are unable to uniquely retrieve the ionosphere in this case. Panel (c) shows the prior ionosphere used; this ionosphere has a structure that is similar to the input ionosphere but has a higher magnitude ~3x the initial volume emission rate. Panel (d) shows the retrieved volume emission rate initialized with the prior from panel (c). This simulation shows that a reasonable prior ionosphere is needed to help the technique, both the observations and the inversion method, converge to a physical ionosphere. Figure 5 shows the electron densities derived by completing the full inversion, as outlined above, of the simulated data for the first simulation using a nominal IRI-2007 ionosphere. Panel (a) shows the input electron density. The prior density used in the inversions is shown in panel (b); this prior has a similar structure to the Input Density but a much larger magnitude. A Maximum A Posteriori (MAP) retrieval [*Kamalabadi*, 2010] that assumed the uncertainty of the prior ionosphere is 20% of the electron density is shown in panel (c) and the LSPD retrieval is shown in panel (d). MAP retrievals include uncertainties from the model and the data in the inversion. Where the uncertainties in the data are large, the MAP retrieval will tend toward the model, but, in regions where the data uncertainties are less than the model uncertainties, the retrieval will be driven by the data. The MAP retrieval is similar to the LSPD retrieval and reflects that the assumed uncertainty assumed for the model was too large and therefore the retrieval was driven by the measurement uncertainties. Figure 6 shows the percentage differences between the input electron density and the prior, LSPD retrieval, and MAP retrievals for the nominal IRI-2007 ionosphere. Panel (a) shows the (Prior – Input electron density)

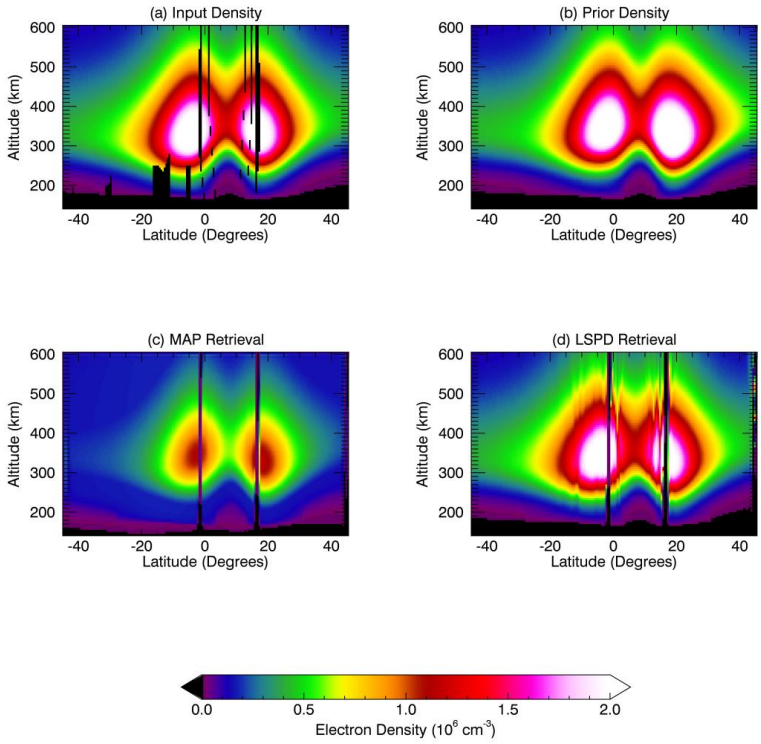

Figure 7: The electron densities for the ionospheric bubble simulation are shown. Panel (a) shows the input electron density. The prior density used in the inversions is shown in panel (b); as noted above, this prior has a similar structure to the Input Density but the northern peak of the EIA is larger in magnitude and displaced northward. The MAP retrieval is shown in panel (c) and the LSPD retrieval is shown in panel (d). The MAP retrieval has a lower magnitude than the Input Density and only the most prominent bubbles are reproduced. The LSPD retrieval is in better agreement with the Input Density however the smaller bubbles and those on the bottomside are not reproduced. Several "line artifacts" are also present in the reconstruction; this type of artifact is caused by the algorithm.

divided by the input electron density. The prior electron density was larger everywhere except in the valley below the magnetic equator indicated by the blue region. The contours in the images are at -10%, 0%, and +10%. The percentage difference between the MAP retrieval and input density is shown in panel (b) and the percentage difference between LSPD retrieval and the input density is shown in panel (c). The LSPD retrieval is within ±10% of the input density almost everywhere except, most notably, on the bottomside.

Figure 7 shows the electron densities for the ionospheric bubble simulation. Panel (a) shows the input electron density, which is an IRI-2007 ionosphere with bubbles superimposed. The prior density used in the inversions is shown in panel (b); as noted above, this prior has a similar structure to the Input Density but the northern peak of the EIA is larger in magnitude and displaced northward. The prior was derived by using an ionosphere IRI-2007 ionosphere at the same local time and geophysical conditions but 45° eastward in longitude of the ionosphere used in the simulation. The MAP retrieval is shown in panel (c) and the LSPD retrieval is shown in panel (d). The MAP retrieval has a lower magnitude than the Input Density and only the most prominent bubbles are reproduced. The LSPD retrieval is in better agreement with the Input Density however the smaller bubbles and those on the bottomside are not reproduced. Several "line artifacts" are also present in the reconstruction; this type or artifact is caused by the algorithm. These line artifacts can presumably be removed using upgrades to the retrieval algorithm [*Frikel and Quinto*, 2013]. Figure 8 shows the percentage differences between the input electron density and the prior, LSPD retrieval, and MAP retrievals for the ionospheric bubble simulation. Panel (a) shows the (Prior – Input electron density) divided by the input electron density. The prior electron density shows a different morphology than the Input Density and does not contain any bubbles. The percentage difference between the MAP retrieval and input density is shown in panel (b) and the percentage difference between LSPD retrieval and the input density is shown in panel (c). The MAP retrieval differs everywhere from the Input. The LSPD retrieval is within ±10% of the input density almost everywhere

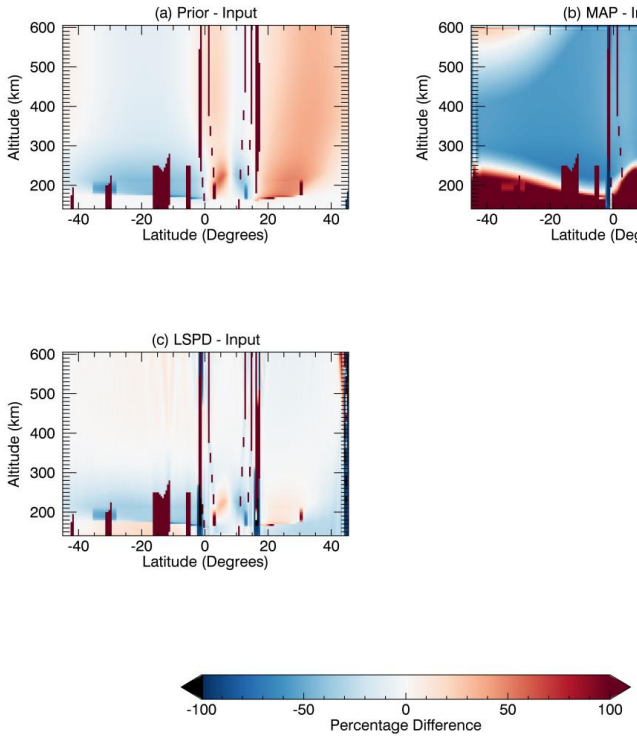

Figure 8: The percentage differences between the input electron density and the prior, LSPD retrieval, and MAP retrievals are shown for the ionospheric bubble simulation. Panel (a) shows the (Prior – Input electron density) divided by the input electron density. The prior electron density shows a different morphology than the Input Density and does not contain any bubbles. The percentage difference between the MAP retrieval and input density is shown in panel (b) and the percentage difference between LSPD retrieval and the input density is shown in panel (c). The MAP retrieval differs everywhere from the Input. The LSPD retrieval is within ±10% of the input density almost everywhere except, most notably, in the bubbles. The density of the bubbles in the retrieval is larger than it is in the Input Density.

except, most notably, in the bubbles. The density of the bubbles in the retrieval is larger than it is in the Input Density, which suggests that the algorithm is shifting photons from areas of higher emission rate into the bubbles. This may be a consequence of the diffusion based regularization approach used in VERT.

5. Summary and Conclusions

The CIRCE mission, the UV instrumentation, some observation scenarios, and preliminary demonstrations of mission effectiveness were presented and discussed. The simulations used realistic viewing geometries, with expected instrumental sensitivities, and realistic noise was superimposed to create simulated "data", which were then inverted using the Volume Emission Rate Tomography technique. We assessed the accuracy of the retrievals given that the observational scenarios produce the typically underdetermined problems encountered in ionospheric tomography. The simulations and retrievals included the full physics of ionospheric 135.6 nm nightglow including the radiative recombination and mutual neutralization sources, vertical radiation transport (except in the bubble simulations), and radiation transfer along the lines-of-sight. These simulations demonstrate that the CIRCE mission is able to retrieve the ionospheric structure given a reasonable prior ionosphere. The simulations also demonstrated that the ionospheric morphology is well-captured including small-scale structures such as ionospheric bubbles. Research is continuing on how to determine the least biased prior ionospheres for use in the inversions.

Acknowledgements: The Chief of Naval Research supported this work through the Naval Research Laboratory (NRL) 6.1 Base Program.

5. References

Anthes, R. A., et al. (2008), "The COSMIC/FORMOSAT-3 Mission: Early Results", *Bull. Amer. Meteor. Soc.*, 313-333, DOI:10.1175/BAMS-89-3-313.

Bilitza, D., and B. W. Reinisch (2008), "International Reference Ionosphere 2007: Improvements and new parameters", *Adv. Space Res*., 42, 599–609, doi:10.1016/j.asr.2007.07.048.

Dymond, K. F. (2009), "Remote sensing of nighttime F region peak height and peak density using ultraviolet line ratios", *Radio Sci*., 44, RS0A28, doi:10.1029/2008RS004091.

Dymond, K. F., et al. (2016), "The Tiny Ionospheric Photometers on the COSMIC Constellation", *J. Geophys. Res. Space Physics*, 121, doi: 10.1002/2016JA022900.

Dymond, K. F., et al (1997), "An Optical Remote Sensing Technique for Determining Nighttime F–Region Electron Density", *Radio Sci*., Vol. 32, No. 5, 1985-1996.

Dymond, K. F. and R. J. Thomas (2001), "An algorithm for inferring the two–dimensional structure of the nighttime ionosphere from radiative recombination measurements", *Radio Sci*., Vol. 36, No. 5, 1241-1254.

Dymond, K. F., S. A. Budzien, and M. Hei (2017), "Ionospheric-Thermospheric UV Tomography: 1) Image Space Reconstruction Algorithms", *Radio Sci*., doi: 10.1029/2015RS005869.

Dymond, K. F., J. B. Nee, and R. J. Thomas (2000), "The Tiny Ionospheric Photometer: An Instrument For Measuring Ionospheric Gradients For The COSMIC Constellation", in "Applications of the Constellation Observing System for Meteorology, Ionosphere, and Climate", p 273-290, Springer, New York, New York.

Frikel, J. and Quinto, E. T. (2013), *Inv. Prob*., 29, 125007, doi: 10.1088/0266-5611/29/12/125007.

Kamalabadi, F. (2010), Multidimensional image reconstruction in astronomy: A unified approach based on regularization and state estimation concepts, *IEEE Signal Processing Magazine*, Vol. **86**, 86-96, doi: 10.1109/MSP.2009.934717.

Meier, R. R. (1991), "Ultraviolet Spectroscopy and Remote Sensing of the Upper Atmosphere", *Space Sci. Rev*., 58, 1-186.

Meléndez-Alvira, D. J., et al. (1999), "Analysis of the oxygen nightglow measured by the Hopkins Ultraviolet Telescope: Implications for ionospheric partial radiative recombination rate coefficients", *J. Geophys. Res*., 104(A7), 14901–14913, doi:10.1029/1999JA900136.

Picone, J. M., et al. (2002), "NRLMSISE-00 empirical model of the atmosphere: Statistical comparisons and scientific issues", *J. Geophys. Res*., 107(A12), 1468, doi:10.1029/2002JA009430.

Press, W. H., et al. (1992), "Numerical Recipes: The Art of Scientific Computing", Cambridge University Press, New York, NY.

Tsunoda, R. T., et al. (1979), Altair: an incoherent scatter radar for equatorial spread F studies, *Radio Sci*., 14(6), 1111–1119, doi:10.1029/RS014i006p01111.

Wang, J., et al. (1987), Effects of the Close Approach of Potential Curves in Photoabsorption by Diatomic Molecules—II. Temperature Dependence of the O2 Cross Section in the Region 130–160 nm, *J. Quant. Spectroscopy and Radiative Transfer*, 38, 19.